Materials Advances

ROYAL SOCIETY OF CHEMISTRY

PAPER

View Article Online
View Journal | View Issue

Cite this: *Mater. Adv.*, 2026, 7, 1568

Bioinspired superhydrophobic surfaces for anti-corrosion and drag reduction using additive manufacturing for marine applications

Aaishwarika Raj Sharma, Harpreet Arora and Harpreet Singh Grewal *

Nature offers exquisite examples of superhydrophobicity, yet replicating their intricate geometries remains challenging with conventional manufacturing techniques. In this study, bioinspired intricate surface geometries were fabricated using additive manufacturing with flame spraying to impart nano-scale hierarchical roughness essential for sustained de-wetting performance. The complex geometries inspired from different superhydrophobic surfaces such as a lotus leaf, taro leaf, springtail, and butterfly wings were created on 17-4 PH stainless steel using powder bed fusion. Furthermore, the additive textures were adorned with micro-nano roughness generated through aluminium flame spraying. The influence of surface geometry on de-wetting, durability, corrosion, and drag reduction behaviour was studied. Post-silanization, the lotus-inspired flame-sprayed (LFS) sample morphology exhibited superior de-wetting properties, with dynamic contact angles of 158° and 156°, and a low sliding angle of 5°. This sample demonstrated high mechanical durability by maintaining superhydrophobicity for more than 6000 abrasion cycles at 5 kPa, with the unique trait of self-regeneration. Additionally, it resisted liquid impact for over 120 minutes in simulated rain at 4 m s^{-1} and displayed a low corrosion current density of 0.3 μA cm^{-2}, indicating improved corrosion resistance. The coating demonstrated superior drag reduction for water, and low surface tension for liquids and oil, with drag 21 times lower than substrate for water. This study advances the practical applicability of superhydrophobic coatings and bridges the gap between lab-made prototypes and scalable industrial applications with high durability accompanied by superior anti-drag and anti-corrosion characteristics.

Received 27th October 2025,
Accepted 17th December 2025

DOI: 10.1039/d5ma01236h

rsc.li/materials-advances

1. Introduction

Superhydrophobicity is found in different species in the biological kingdom, starting from the plants to the insects. Distinct micro- and nano-structures that assist in efficient water repellency are found in the lotus leaf and taro leaf, as well as butterfly wings. In the same manner, the water strider uses hydrophobic body hair to walk on water surfaces, and the springtail possesses an omniphobic cuticle that repels a wide range of liquids, keeping this insect dry.[1–3] The high contact angles ($>150^\circ$) and low sliding angle ($<5^\circ$) with extremely low contact angle hysteresis promote water-repellent behaviour on such surfaces. This unique trait influences the anti-corrosion,[4] low drag,[5] self-cleaning,[6] anti-staining,[7] and anti-icing[8] behaviour of surfaces.

There is great potential in engineering and industrial applications for metallic superhydrophobic surfaces and others exhibiting versatility. Superhydrophobic surfaces, characterized by their outstanding de-wetting characteristics, hold a promising solution to numerous industrial challenges arising from solid–liquid contact. In the marine industry, there is huge potential for these surfaces to counteract the two major global challenges of corrosion and drag.[9] Corrosion causes the loss of structural integrity and lifespan in systems, whereas excessive drag substantially lessens efficiency through increased fuel utilization. These combined problems result in high maintenance expenditures, high emissions, and ecological issues.

Maritime ships serve a critical function in international trade by carrying more than 90% of merchandise across the globe.[10] The escalation of the volume of transportation and its attendant emissions, however, presents severe environmental concerns. Heavy fuel oil, which is widely utilized on seas, contributes enormously to the emission profile of the transport sector, representing approximately 2.9% of the total CO_2 equivalent in 2022.[11] In addition, the drag forces on seagoing vessels and fluid pipeline transport increase fuel consumption and CO_2 emissions, further aggravating global warming. By reducing corrosion and drag, superhydrophobic surfaces have

Surface Science and Tribology Lab, Department of Mechanical Engineering, Shiv Nadar Institution of Eminence, Gautam Buddha Nagar, Uttar Pradesh 201314, India. E-mail: harpreet.grewal@snu.edu.in

the potential to improve fuel efficiency, lower emissions, and reduce environmental impacts. This new technology presents a green method forward for the shipping industry to tackle the urgent issues of efficiency and ecological preservation.

Researchers are working on many approaches such as hydrothermal,[12] electrodeposition,[13] etching,[14] and compression moulding[15] for the fabrication of superhydrophobic surfaces. However, these techniques produce a random surface morphology and limit what can be customized and shaped regarding surface textures. To create bioinspired textured surfaces, it is necessary to reproduce very intricate functioning architecture with multiscale surface roughness, and low surface energy materials. This requires the use of sophisticated engineering techniques, which will ensure durability and proper functioning. Methods such as photolithography and additive manufacturing (AM) can be used to create customized textures. Photolithography involves the use of light to create desired patterns with nanometric precision.[16] However, it is restricted to two-dimensional (2D) flat surfaces, which limits its applicability on twisted and curved surfaces. Although popular in the semiconductor industry for micro-nano fabrication on chips, scaling photolithography for engineering applications is expensive and unfeasible.

Three-dimensional (3D) printing, also known as AM, is revolutionizing many industries with its ability to precisely manufacture custom parts with complex geometries. This innovative technology provides unparalleled design flexibility, as well as much more efficient use of material with lower waste and production costs.[17] AM enhances the functionality of materials by creating new possibilities to texture surfaces, as well as design structures, and creates entire new opportunities that go far beyond simple structural fabrication. AM facilitates efficient and facile fabrication of complex and intricate surface textures, providing a potential means for tuning surface properties.[18] Bioinspired superhydrophobic functional surfaces can be fabricated by designing similar surface textures through AM.

In recent years, researchers have fabricated superhydrophobic surfaces by crafting micro-textures through AM, and have investigated their wetting behaviour and surface functionality. Sun *et al.*[19] used selective laser melting (SLM) to create inverted trapezoidal structures on SS316. A comparative study of untreated, naturally aged, and heat-treated samples indicated that the contact angles of heat-treated samples were high due to the adsorption of organic hydrocarbons, with the maximum contact angle obtained for chemically modified samples. Corrosion resistance was related to better wetting behaviour; however, superhydrophobic samples possessed poor abrasion resistance, losing superhydrophobicity after 40 minutes of exposure.

Zhang *et al.*[20] explored the effects of laser scanning speed on surface morphologies. Superhydrophobic surfaces were prepared using SLM from TiC/Inconel 718 nanocomposites. Varying the scanning speed between 400 mm s^{-1} and 700 mm s^{-1} with a fixed laser power of 120 W resulted in varied outcomes. A scanning speed of 600 mm s^{-1} generated the maximum contact angle of 151°, which was reduced to 145° at increased speeds. Superhydrophobicity only occurred at a unique scanning speed, and the lowest corrosion current density achieved (10^{-6} A cm^{-2}) was still greater than what is generally anticipated for superhydrophobic surfaces. Furthermore, durability issues of the altered surfaces were not explored.

Mekheil *et al.*[21] manipulated wetting behaviour through partially melted powder particles adhered to the side surfaces of the textures, which resulted in re-entrant structures. The micro-scale second-order structures resulted in a low contact angle of 141°, and showed an inability to attain the superhydrophobic regime. The above studies emphasize the importance of additive manufacturing in tailoring the micron-sized features and versatility to create intricate geometries. However, the integration of sub-micron and nano-sized features continues to be necessary.

The current study draws inspiration from different natural superhydrophobic surfaces. The intricate topography of such surfaces is achieved through additive manufacturing. These additive textures are adorned with two-order hierarchal roughness by aluminium flame spraying. This unique combination leads to the design of three-order hierarchal roughness, contributing to superior de-wetting behaviour. The additive textures reduce the solid–liquid contact, resulting in enhanced air fraction, and hence promoting de-wetting. These textures aid in preserving the flame-sprayed coatings, which otherwise are totally exposed and undergo physical abrasion in the non-textured sample. AM textures have intensively contributed to improving the durability of flame-sprayed superhydrophobic samples. However, the surface geometry of the textures has its own implications in determining the de-wetting and durability. The textured superhydrophobic samples displayed high durability with low drag and corrosion.

2. Experimental section

2.1 Material and process parameters

The feedstock consisted of 17-4 PH stainless steel powder with a particle size of 10–15 μm. The samples were fabricated using DMP Flex 100 with a 100-W continuous laser in an argon environment. The layer thickness and scanning speed were maintained at 30 μm and 1000 mm s^{-1}, respectively. The aluminium powder was purchased from Metallizing Equipment Co. Pvt. Ltd (MECPL), India. The pre-treatment of powder consisted of drying for 12 hours at 80 °C in an oven. A Powderjet 86 – II (MECPL, India) spray gun was used for spraying. The oxygen and acetylene pressure were maintained at 1.1 bar and 2.2 bar, respectively. The pressure of carrier gas nitrogen was 4 bar. The coating was deposited at a 10-inch spraying distance and 1 bar accelerating gas pressure. The chemical modification of the samples was performed with a 1*H*,1*H*,2*H*,2*H*-perfluorooctyltriethoxysilane (FOTES) coating using vapor deposition at 150 °C for 90 minutes.

2.2 Designing and surface texturing

The microstructure of a lotus leaf (*Nelumbo nucifera*), taro leaf (*Colocasia esculenta*), butterfly wings (*Pieris canidia*), and slender springtail (*Entomobrya nivalis*) is shown in Fig. 1(a)–(d).

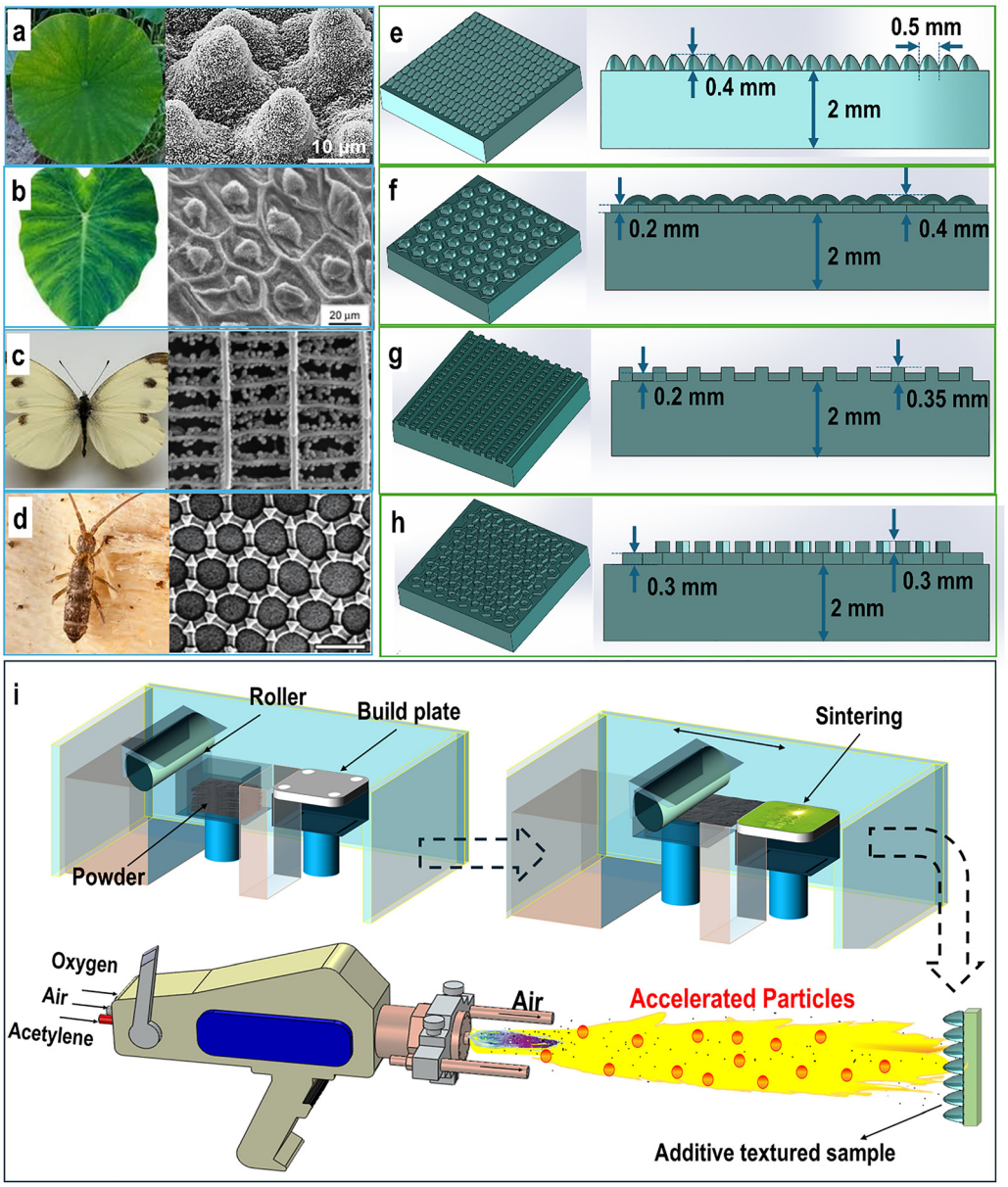

Fig. 1 Fabrication process of bioinspired superhydrophobic coatings. (a)–(d) Microstructures of a lotus leaf (*Nelumbo nucifera*), taro leaf (*Colocasia esculenta*), butterfly wings (*Pieris canidia*), and slender springtail (*Entomobrya nivalis*). (e)–(h) 3D-designed macrographs through SolidWorks, and (i) schematic illustration showing the fabrication of superhydrophobic surfaces through additive manufacturing and flame spraying.

To artificially fabricate these textures, they are first designed in SolidWorks, as shown in Fig. 1(e)–(h). Although the original textures on these species are in the nano-size range, this work is inspired more by the geometry of the textures, and hence is designed on a macro scale. To mimic lotus leaf morphology, hill-like textures were designed by revolving a 0.5-mm length of a D-shaped 2D sketch extruded to a 0.4-mm height. Similarly, the taro leaf textures were designed with a semicircular protrusion extruded to a 0.4-mm height surrounded by hexagonal structures of 0.2-mm height with a thickness of 0.2 mm.

Butterfly wings are another animal kingdom-inspired morphology, and were designed with ridges having a width and height of 0.35 mm with spacing of 0.5 mm. These individual ridges were bridged with small ridges with a width and height of 0.2 mm. The slender springtail inspired the fabrication of a two-order hierarchy with a honeycomb structure (hexagons with 0.3-mm height) decorated with triangular extrusions consisting of two side lengths of 0.5 mm and one side length of 0.34 mm, with a height of 0.3 mm on each of the six edges of the hexagon. The powder bed fusion (PBF) technique was used for additive texturing of these bioinspired features.

These additively manufactured samples were flame-sprayed with an aluminium coating to generate hierarchal roughness. After flame spraying, the different bio-inspired textures were named LFS, TFS, SFS, and BFS, which were designated as lotus-inspired flame-sprayed, taro leaf-inspired flame-sprayed,

springtail-inspired flame-sprayed, and butterfly-inspired flame-sprayed, respectively. Fig. 1(i) shows a schematic of the designs and the fabrication route followed to develop superhydrophobic coatings through additive manufacturing and flame spraying. The cost and material consumption for different textures with the same dimensions are compared in Table 1. The cost analysis for different textures was also calculated based on the material consumption by individual textures.

2.3 Characterization

Field emission scanning electron microscopy (FESEM) (JEOL, JSM-7610FPlus, Japan) with 15 kV acceleration voltage was used to investigate the surface morphology. The surface chemistry of samples was analyzed through X-ray diffraction (XRD) and X-ray photoelectron spectroscopy (XPS) analysis. The XRD analysis was performed with a Panalytical Empyrean X-ray diffractometer with CuKα (0.154 nm) radiation. XPS (Thermo Fisher Scientific) with micro-focused X-rays using a monochromatic Al-Kα source, a hemispherical analyzer, and a 128-channel plane detector was used to analyze the surface chemistry of coatings.

A goniometer (Apex, India) was employed to perform contact angle measurements using the sessile drop method. The dynamic measurements were performed by the continuous measurement technique. The liquid was fed/removed at 1 μL min^{-1} into a 3-μL preplaced drop until a 10-μL drop existed. The sliding angle was measured by placing a 5-μL drop and tilting the stage of the goniometer by 5° at a speed of 4° min^{-1}. A force tensiometer (Sigma 701, Sweden) was used for the adhesion tests. The samples were tested with liquids possessing different surface tensions ranging from 28 mN m^{-1} to 72 mN m^{-1} by mixing different ratios of water and ethanol.

The abrasion resistance of the superhydrophobic samples was evaluated using a Universal Tribometer (Rtec, USA) against a 2000-grade abrasive sheet in reciprocating mode at a nominal pressure of 5 kPa at 2 mm s^{-1} velocity and 3-mm stroke length. The performance of coatings during rain simulation was evaluated at a droplet velocity of 4 m s^{-1}. The outdoor weathering test was performed on samples from June 24 to February 25 at the university, during which time the temperature varied from 48 °C to 5 °C with relative humidity in the 72% to 34% range. The sample was exposed to the summer, rainy, autumn, and winter seasons during this period. The effect of weather on superhydrophobicity was assessed by the water contact angles and sliding angle measurements after every 10 days.

The drag reduction potential of the superhydrophobic samples was investigated by rheological experiments, conducted using a rheometer (Anton Paar, MCR302) equipped with a cone-and-plate measuring system. The angle of the cone used was 2° with a diameter of 25 mm. The substrate and superhydrophobic sample (40 mm diameter) were placed on a Peltier board. The DI water used as a testing liquid at 25 °C was placed between the top surface of the sample and the upper cone plate. Further drag behavior of the substrate, and non-textured and textured samples was explored for different liquids with surface tension varying from 28 mN m^{-1} to 55 mN m^{-1}, and oil with a viscosity of 29 mPa-s and surface tension of 33 mN m^{-1}.

The superhydrophobic coatings and substrate were investigated for their corrosion behavior in 3.5% NaCl solution using a potentiostat (Gamry, 1000E). A potentiodynamic polarization test was performed at a 0.1 mV s^{-1} scan rate with a potential range from −0.15 mV to 0.15 mV, corresponding to the open circuit potential (OCP) recorded for 3600 s. A three-electrode system with Ag/AgCl as the reference electrode, graphite as the counter electrode, and the sample as the working electrode was used for the electrochemical test. The electrochemical impedance spectroscopy (EIS) from 10^5 to 10^{-2} Hz at OCP was recorded with an AC voltage amplitude of 10 mV. The superhydrophobic sample was investigated under dynamic immersion in the wave simulator fabricated in the laboratory using simulated seawater (3.5 wt% NaCl). The change in contact angle was measured at regular intervals to determine the change in de-wetting characteristics. Coffee, tea, fruit juice, tomato sauce, and oil were used as wet contaminants to investigate anti-staining properties.

Table 1 Material and the corresponding cost estimation of the different textures

Bio-inspired texture	Material (cm^3)	Time (min : s)	Cost (USD)
Lotus-inspired texture	2.63	43 : 19	14.85
Taro-inspired texture	2.65	43 : 56	14.97
Springtail-inspired texture	2.77	46 : 39	15.68
Butterfly-inspired texture	2.70	46 : 11	15.31

3. Results and discussion

3.1 Surface characterization

The surface morphology before and after flame spraying is shown at high and low resolution in Fig. 2. The surface morphology of the additively manufactured non-textured samples is shown in Fig. 2(a1) and (a2). The additive manufacturing (AM) approach replicated the bioinspired textures at the macroscale level. The AM produced hill-like features with consistent dimensions of 0.48 ± 0.02 mm in width and 0.72 ± 0.02 mm in length of individual hills inspired by lotus leaf morphology, as shown in Fig. 2(b1). Between every four adjacent hills, saddle-like depressions were formed, resembling curved rhombus-shaped holes with a diagonal length of 0.6 ± 0.04 mm and 0.4 ± 0.08 mm generating one-scale roughness, as shown in Fig. 2(b2).

The taro leaf-inspired morphology was composed of dome-shaped features having an average diameter of 0.8 ± 0.08 mm surrounded by 0.2 ± 0.04 mm thick hexagons and an inter-spatial gap of 0.16 ± 0.02 mm between them, as highlighted in Fig. 2(c1) and (c2). In Fig. 2(d1) and (d2), the springtail-inspired structure consisted of a triangular pillar present on top of each vertex hexagonal ring. The triangle structures were rounded instead of flat due to the surface tension, with two side lengths of 0.25 ± 0.02 mm and one side length of 0.2 ± 0.02 mm. Circular holes inside the hexagon with a diameter of 0.7 ± 0.05 mm were observed. The triangular extrusions in

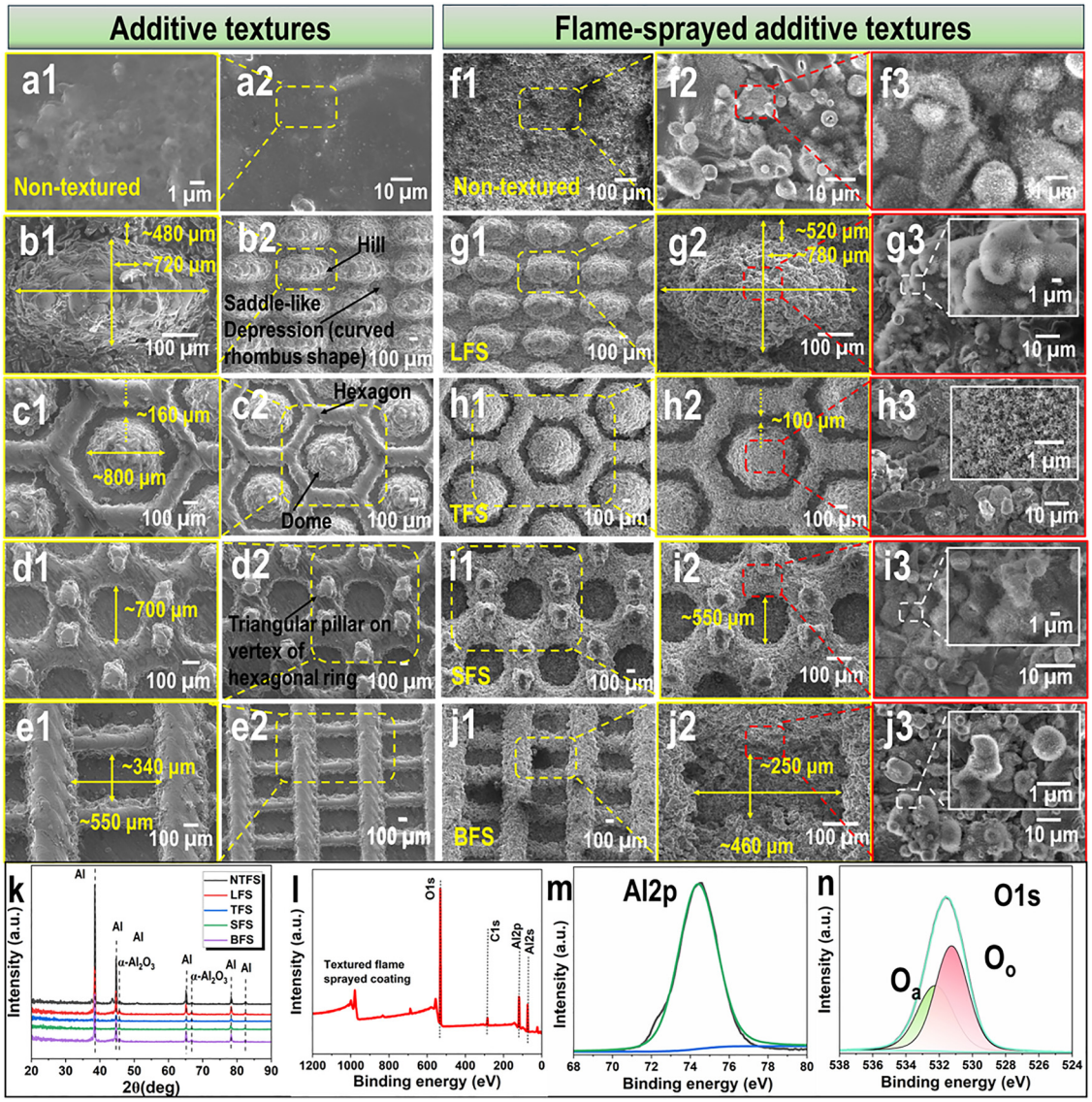

Fig. 2 Surface morphology examined using electron microscopy showing low- and high-resolution micrographs of additively fabricated non-textured and bioinspired textured samples (a)–(e) without flame spraying and (f)–(j) after flame spraying of aluminium. The coating highlighted in the yellow border indicates low-resolution images and in the red border denotes high-resolution images; the insets focus on nano-sponge-like textures developed on microsplats that cover individual additive textures. After the coating of aluminium on textures, the surface chemistry was investigated through (k) X-ray diffraction and (l)–(n) X-ray photoelectron spectroscopy (XPS) techniques.

the springtail-inspired morphology led to a two-tier hierarchy. The butterfly-inspired surface morphology consisted of prominent linear ridges interlinked by a network of secondary ridges with a comparatively lower height, as highlighted in Fig. 2(e1) and (e2). Rectangular pockets were created in-between with a size of approximately 0.34 mm × 0.55 mm, as shown in Fig. 2(e1).

Further these microscale textures were decorated with micro-nano structures through flame spraying. The aluminium was flame-sprayed at a high spraying distance of 10 inches, which leads to nanostructure formation due to a low melting and vaporization temperature.[22] To achieve multi-order hierarchy, the two popular industrial techniques were combined, aiming at scalability for superhydrophobic surfaces. Fig. 2(f1)–(f3) shows non-textured flame-sprayed additively manufactured samples (NTFSs). The 5-μm to 30-μm-sized microsplats are covered nanostructures with 5 nm to 20 nm of nanopores. After flame spraying on bioinspired additively manufactured textures, the aluminium coating was uniformly deposited. These samples were designated as LFS, TFS, SFS, and BFS for lotus leaf, taro leaf, springtail, and butterfly wing-inspired morphology, respectively.

The hills and valleys in LFS were covered with micro-nano structures throughout, as seen in Fig. 2(g1) and (g2), which shows that the nanosponge-like structures were created on individual splats. After aluminium coating deposition, the length and width of single hill features increased to 0.78 ± 0.02 and 0.52 ± 0.02, respectively, as marked in Fig. 2(g2). In TFS,

the aluminium coating was uniformly deposited on hexagon- and dome-shaped protrusions, and there was a quantitive increase in the thickness of hexagons from 0.2 ± 0.04 mm to 0.3 ± 0.06 mm, as seen in Fig. 2(h1) and (h2). The gaps between dome-shaped features and hexagons were reduced to 0.1 ± 0.02 μm from 0.16 ± 0.02 μm (Fig. 2(h2)).

Aluminium coating deposition occurred on two-tier structures for SFS. The diameter of circular holes inside the hexagon was reduced to 0.55 ± 0.02 mm from 0.7 ± 0.05 mm, as seen in Fig. 2(i1) and (i2). In BSF, the average size of the rectangular pockets (0.25 mm × 0.46 mm) was reduced, which was attributed to the uniform aluminium deposition throughout the structures, as shown in Fig. 2(j1) and (j2). The nanostructures of all geometries were visible, illustrating the nano-sponge like morphology as identified in high-resolution FESEM images Fig. 2(f3)–(j3).

The surface chemistry of non-textured and textured samples after flame spraying was studied by X-ray diffraction (XRD) and X-ray photoelectron spectroscopy (XPS). From XRD analysis, pure aluminium peaks were observed with minor peaks of α-Al_2O_3, which reflects the partial oxidation (Fig. 3(k)). While flame spraying, the samples were maintained at a high spraying distance, and the aluminium powder particles travelling along the flame were oxidized. XPS was used to confirm the oxidation and formation of α-Al_2O_3. The survey spectra show major peaks of Al2p, Al2s, O1s, and C1s, as shown in Fig. 3(l). The high resolution de-convoluted peaks of Al2p and O1s are shown in Fig. 3(m) and (n), respectively. For Al2p, a peak was observed at 74.6 eV, and for O1s, peaks were observed at 530 eV and 532 eV, representing oxide oxygen and absorbed oxygen peaks. The formation of these peaks at the respective binding energy indicates the presence of α-Al_2O_3.[23,24]

3.2 Wetting behaviour

The wetting behaviour of non-textured and textured samples was analyzed through goniometry by measuring dynamic and sliding angles, as shown in Fig. 3(a). The NTFS sample demonstrated a low advancing angle of 152° and receding angle of 150°. The dynamic contact angles increased for the textured coatings, the highest being displayed by LFS with an advancing angle of 158° and a receding angle of 156°, followed by TFS, SFS, and BFS. TFS demonstrated an advancing angle of 156° and a receding angle of 154°. The advancing angles of SFS and BFS were 155° and 152°, with receding angles of 153° and 150°, respectively.

To ensure the stability of the entrapped air layer, the superhydrophobic samples were tested against liquids with different surface tensions varying from 28 mN m^{-1} to 55 mN m^{-1}. The static contact angles were measured, as shown in Fig. 3(b). The contact angles decreased for low surface tension liquids because they spread due to weak cohesive forces. However, it was observed that the textured coatings, especially LFS and TFS, resisted spreading and demonstrated a high contact angle for liquids up to 33 mN m^{-1} surface tension. The LFS coating demonstrated the lowest adhesion of 2.8 μN, followed by TFS, with an adhesion of 4.2 μN, as shown in Fig. 3(c) and (d). NTFS, SFS, and BSF exhibited a comparatively higher adhesion force.

The geometry plays a significant role in determining the adhesive force of the surface. In the case of LFS and TFS, the solid tips come into initial contact with the water droplet when snapped in on the surface.

These tips, especially for LFS, which is composed of hill-like structures, offer minimum friction compared to all other counterparts. The adhesion force can also be visualized for all textured samples in Fig. 3(e)–(h), where the water droplet is elongated at the time of pullout, which shows that the surface offers high adhesion. In the case of BSF and SFS, there is greater contact of the solid part, which increases the friction with sagging of the contact line due to a high interspatial distance.

The solid–liquid (f_{sl}) fraction significantly influences the contact angle, as explained by Cassie–Baxter in eqn (1), where R_f denotes the roughness factor, which is the ratio of wetted area (A_{sl}) to flat area (A_f):

$$\cos\theta_{CB} = R_f f_{sl}\cos\theta - (1 - f_{sl}) \quad (1)$$

The solid fraction was measured using the image analysis software ImageJ. The low solid fraction of 22.32%, 37.55%, and 42.86% by SFS, LFS, and TFS, respectively, was attributed to high dynamic contact angles and low sliding angles. The BFS sample exhibited a high solid fraction of 59.29%, resulting in low dynamic contact angles compared to the other textured samples. The solid–liquid fraction influences the adhesion behavior of the surface, and as experimentally observed, LFS demonstrated minimum adhesion. For a composite interface, the adhesion hysteresis (ΔW) is proportional to the liquid–solid area, as shown in eqn (2), where ΔW_0 denotes adhesion hysteresis on a smooth surface:

$$\Delta W = f_{sl} R_f \Delta W_0 \quad (2)$$

The adhesion hysteresis also affects the contact angle hysteresis (CAH), along with other influencing factors such as surface roughness and heterogeneities, as shown in eqn (3) and (4):[25]

$$\cos\theta_{adv} - \cos\theta_{rec} = \frac{\Delta W}{\gamma_{la}} \quad (3)$$

$$\cos\theta_{adv} - \cos\theta_{rec} = \frac{f_{sl} R_f \Delta W_0}{\gamma_{la}} \quad (4)$$

The above equations clearly state the dependence of the solid–liquid fraction on contact angles, adhesion hysteresis, and CAH. Additive textures significantly aid in reducing the solid–liquid fraction, which is further influenced by the different geometries of these textures.

3.3 Durability studies

3.3.1 Mechanical durability. Mechanical durability, one of the crucial aspects of superhydrophobic coatings, was tested against 2000 grit silicon carbide (SiC) sandpaper at a pressure of 5 kPa. The dynamic contact angles along with sliding angles were measured after each abrasion cycle. The textured flame-sprayed samples retained superhydrophobicity for a significantly longer period than the non-textured flame-sprayed sample, as observed in Fig. 4. The NTFS coating sustained high contact angles and low sliding angles for 1600 abrasion cycles (Fig. 4(a)).

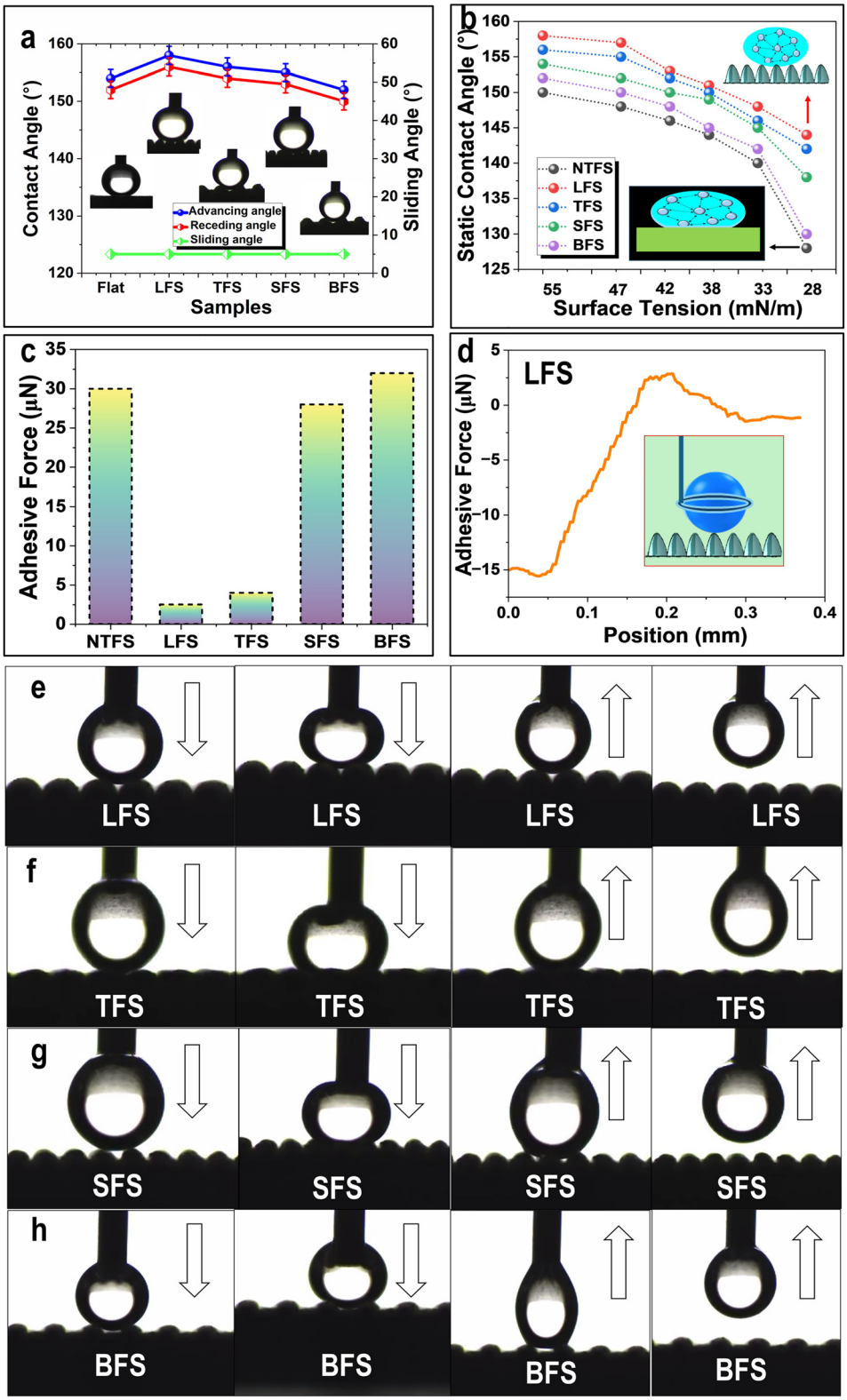

Fig. 3 Investigation of the wetting behaviour of non-textured and bioinspired textured coatings. (a) Dynamic and sliding contact angle measurements. (b) The static water contact angles of liquids with different surface tensions (28 mN m^{-1} to 72 mN m^{-1}) to investigate the stability of the Cassie–Baxter state. The results of the droplet-superhydrophobic surface interactions showing the (c) adhesion force and (d) force-displacement plot, and (e)–(h) snapshots visualizing surface adhesion of a water droplet to textured superhydrophobic surfaces, showing the low adhesion and resistance to water penetration.

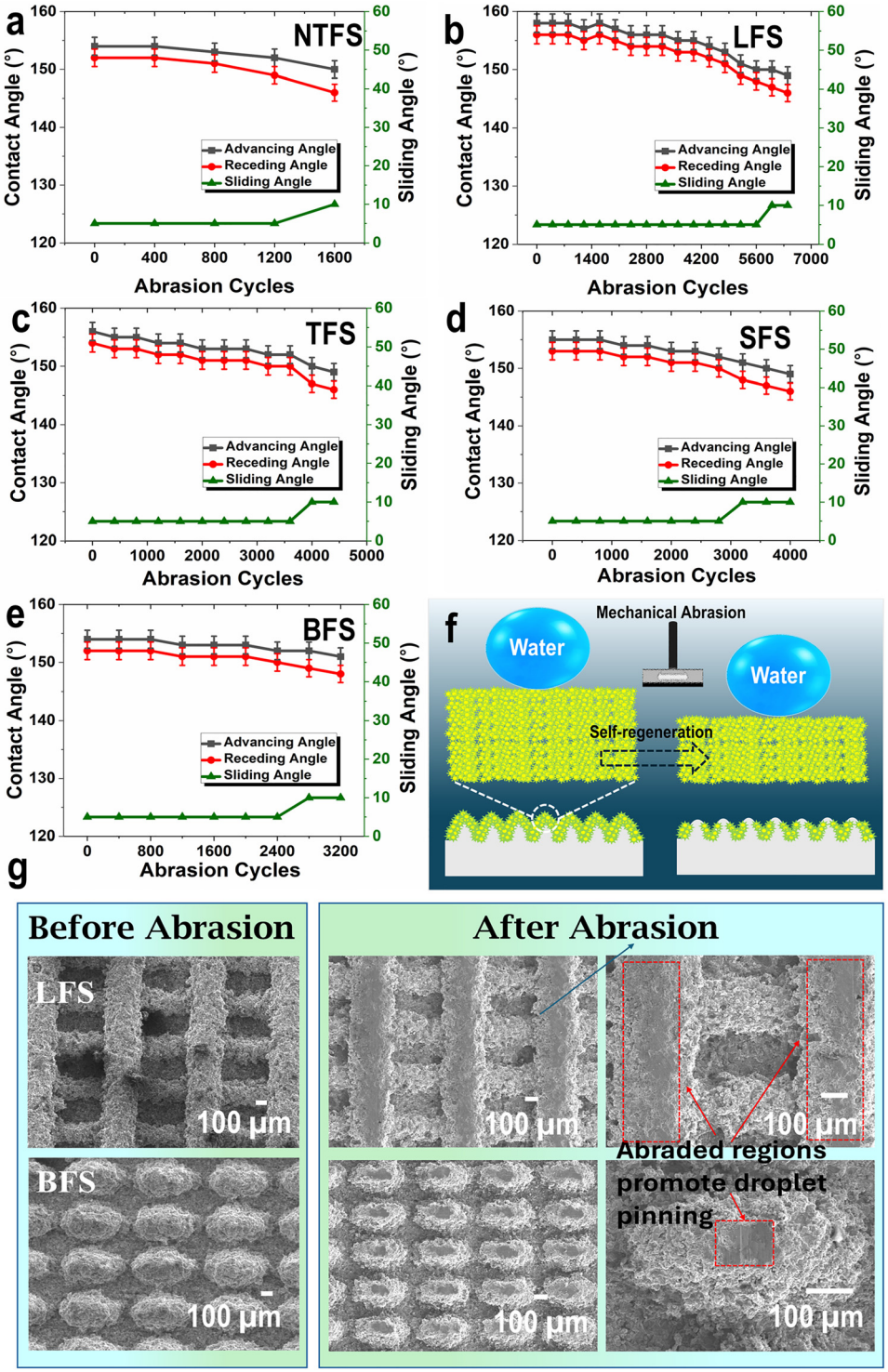

Fig. 4 Mechanical durability evaluation of the non-textured and bioinspired textured superhydrophobic samples showing the change in dynamic contact angles and sliding angle measured during abrasion at 5 kPa for the (a) non-textured flame-sprayed coating (NTFS), (b) LFS, (c) TFS, (d) SFS, and (e) BFS. (f) Schematic illustration of the abrasion mechanism for LFS coatings showing how textures preserve flame-sprayed coatings and explaining the self-regeneration trait of superhydrophobic coatings. (g) Micrographs of LFS and BFS samples before and after abrasion.

Among the textured coatings, the LFS coating exhibited the highest mechanical durability by retaining superhydrophobicity for 6200 abrasion cycles, followed by TFS for 4800 cycles and SFS for 4400 cycles, and slightly lower for BFS with 3200 cycles (Fig. 4(b)–(e)). For the NTFS sample, the entire coating surface was exposed to an abrasive sheet, and after prolonged abrasion, the substrate was exposed. The additive textures in textured coatings aid in preserving the aluminium coating deposited through flame spraying.

The geometry of textures plays a critical role in the abrasion of deposited coatings. Only a solid that is in contact with the abrasive sheet undergoes abrasion. Among the various bioinspired topographies, LFS exhibited the least solid contact with the abrasive sheet. In the case of the LFS sample, only the superhydrophobic solid tips were exposed to abrasion, while the coating on the remainder of the hill-like structure remained intact, as illustrated in Fig. 4(f).

Conversely, for the BSF sample, the entire rectangular channel was affected by abrasion. To observe the abraded regions, the coatings were examined using scanning electron microscopy, and micrographs of LFS and BFS before and after abrasion were analyzed in Fig. 4(g). Abrasion smooths the surface, eliminating roughness and causing water droplets to pin due to the absence of superhydrophobicity on the flat abraded regions. Furthermore, the coatings sustain high contact angles for longer duration due to the unique trait of self-regeneration, as shown in Fig. S1a.

The flame-sprayed coatings repeatedly restore their chemical and physical properties even after removal of the topmost layer. The next exposed layer after abrasion exhibited superhydrophobic characteristics in the abraded layer. This unique self-regeneration was attributed to the coating deposition mechanism during flame spraying. The melting and vaporization temperature of aluminium is lower than the flame temperature, and this promotes vaporization of molten aluminium particles. The vapors travel the flame and re-nucleate, resulting in a nanosponge-like morphology. This mechanism is explained in detail by our group in a previous study.[7]

Among all the textured samples, LFS has shown superior durability even when compared to previous studies. Li *et al.*[26] discovered that a superhydrophobic sample maintained high contact angles for 2000 abrasion cycles when abraded against a 2000 SiC sheet at 3.3 kPa. Meng *et al.*[27] fabricated a superhydrophobic surface for PCB that showed abrasion resistance for 325 cycles when tested against a 600 SiC sheet under a 1000 g load and distance of 8 cm per abrasion application. Zhang *et al.*[28] fabricated a sample that retained superhydrophobicity for 200 abrasion cycles against a 1000 SiC sheet under a load of 200 g weight, with a back-and-forth distance of 10 cm covered per cycle. The combination of additive texturing with flame spraying resulted in further enhancement of durability, which is very important for bridging the gap between the laboratory and practical applications for superhydrophobic surfaces.

3.3.2 Liquid impact durability. To test the durability of superhydrophobic samples for real world scenarios, the coatings were evaluated in a simulated rain environment at 4 m s^{-1} rain velocity. For NTFS, the dynamic contact angle decreased after 40 min of rain impact, as seen in Fig. 5(a). The textured samples endured liquid impact for the highest duration of 120 minutes for LFS, followed by 90 minutes for TFS (Fig. 5(b) and (c)). The SFS and BSF samples were able to resist liquid impalement for 80 minutes and 70 minutes, respectively, as shown in Fig. 5(d) and (e).

The entrapped air results in negative capillary pressure that can resist the water hammer pressure of impacting rain droplets. The water hammer pressure was measured to be 1.2 MPa using $P_{wh} = 0.2 \times \rho \times C \times v$, where ρ denotes density, C denotes the speed of sound in water, and v denotes the velocity of a droplet. The nanostructures with nanopore size ranging from 10 nm to 50 nm generated a high negative capillary pressure of 2.8 MPa, as calculated using eqn (5):

$$P_c = \frac{-4\gamma_{lv}\cos\theta_{adv}}{d} \quad (5)$$

Due to high negative capillary pressure, the nanostructures resisted the impalement of water droplets, as explained through the schematic in Fig. 5(f). However, the geometry of the additive textures also plays a significant role. In BSF and SFS, the closed rectangular and circular macropores act like pits. Prolonged, repeated impacts from raindrops can damage the nanostructures, creating minute defects that allow droplets to penetrate. Once penetrated, the water becomes trapped in these pits, reducing the surface's superhydrophobicity over time. In contrast, LFS does not have closed pits; its hill-like structures enable droplets to easily slide and roll off, ensuring long-term durability (Fig. 5(g) and (h)).

3.4 Drag reduction

The drag reduction of non-textured and additively textured flame-sprayed coatings was investigated through torque measurements, with a shear rate ranging from 50 to 150 s^{-1} at a controlled temperature of 25 °C in a rheometer. Fig. 6(a)–(e) shows the torque recorded at different shear rates for the superhydrophobic coatings and substrate. In the rheometer, the upper cone plate rotates and produces a velocity gradient of liquid from top to bottom.

The torque measurement indicates the force required to drag the liquid on the surface of the test sample. The high torque value indicates that additional effort is required to drag the liquid on the surface. A lower torque value highlights the reduced effort for liquid movement on the surface, primarily due to positive slip length. All measurements were recorded 3 times for each sample to ensure repeatability. An average torque of approximately 1.3 μNm was recorded for the substrate, whereas for all superhydrophobic samples, the average torque was significantly low. The non-textured superhydrophobic samples exhibited an average torque of 0.16 μNm. The bioinspired additive textures further aided in lowering the torque due to decreased solid–liquid contact. The lowest average torque was recorded for LFS (0.06 μNm), which is 21 times lower than that of the substrate. The recorded average torque

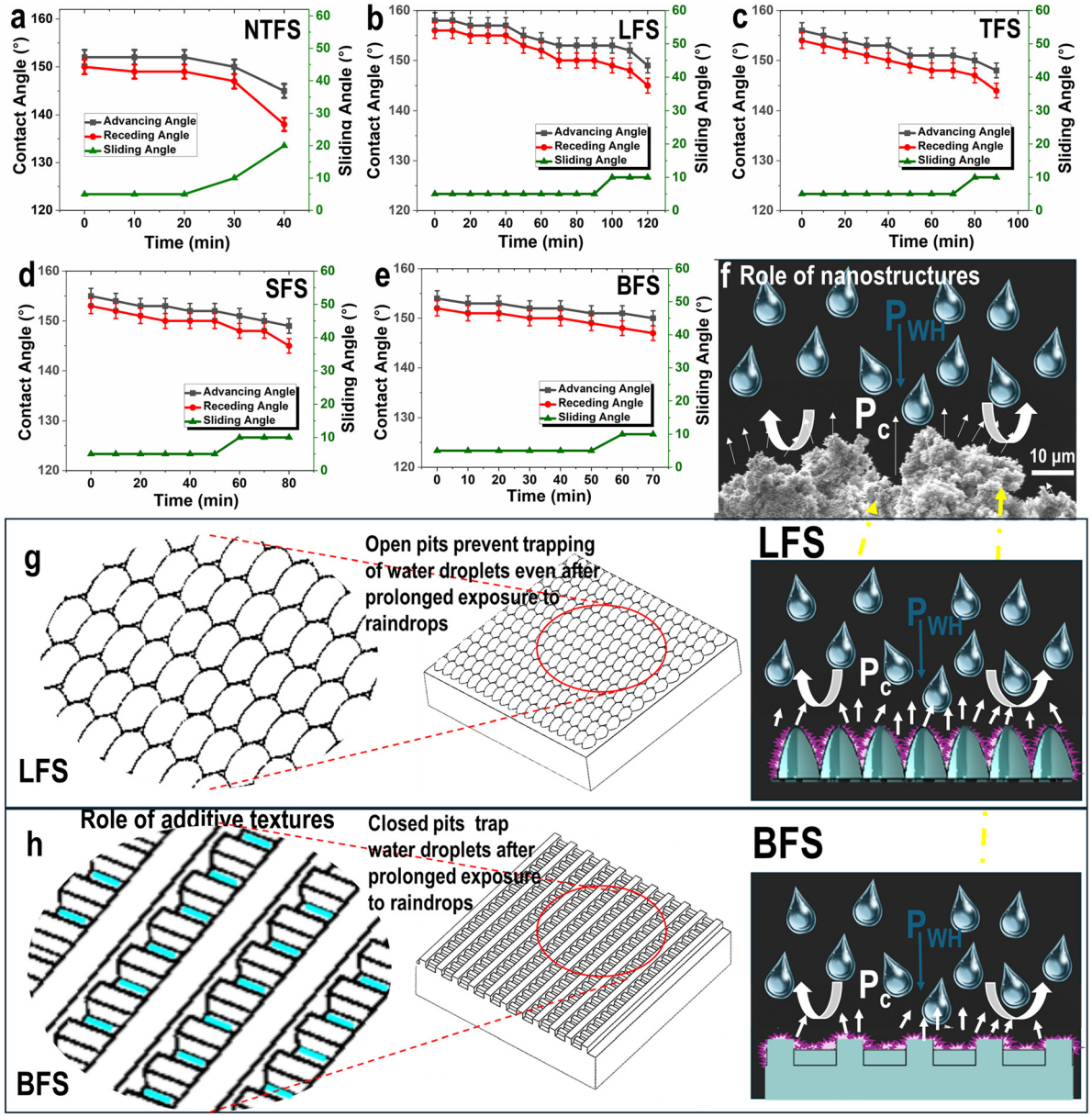

Fig. 5 The performance assessment of superhydrophobic samples under simulated rain at a velocity of 4 m s^{-1}, showing the change in the dynamic contact angles and sliding angle for (a) NTFS, (b) LFS, (c) TFS, (d) SFS, and (e) BFS. (f) Capillary pressure generated due to the entrapped air in nanopores, which enables water droplets to resist impalement while opposing water hammer pressure by rain droplets, as explained through the schematic. Schematic explaining the role of the surface geometry of bioinspired additive textures after prolonged rain impact: (g) LFS with open pits prevents water entrapment, and (h) BFS with closed pits entraps water.

values for TFS, SFS, and BFS were 0.08 μNm, 0.07 μNm, and 0.09 μNm, respectively.

The slip length measurement is another ideal parameter to examine in the study of the drag behaviour of surfaces. The enhanced slip length prevents slip boundary conditions that were earlier an inherent assumption in the case of solid–liquid contact. The slip length was calculated by the Navier–Stokes equation, with Navier's slip boundary condition[29] (eqn (6)):

$$M = \frac{2\pi\mu\omega R^3}{3\theta_0}\left[1 - \frac{3b_{slip}}{2R\theta_0} + \frac{3b_{slip}^2}{R^2\theta_0^2} - \frac{3b_{slip}^3}{R^3\theta_0^3}\ln\left(\frac{R\theta_0 + b_{slip}}{b_{slip}}\right)\right] \quad (6)$$

where M denotes torque; μ denotes viscosity; ω, R, and θ_0 denote the angular velocity, radius, and angle of cone, respectively; and b_{slip} denotes the slip length. Due to inherent water repellency, all superhydrophobic samples displayed a positive slip length varying from 218 μm to 220 μm. The enhanced slip length of the LFS sample is compared with the substrate in Fig. 6(f). In the case of Couette flow, the air layer separates fluid through the solid superhydrophobic protrusions, as shown in Fig. 6(g). As fluid primarily moves over air, the liquid is likely to encounter minimal friction while flowing along the solid surface. If we neglect the solid protrusions (an ideal case), the slip

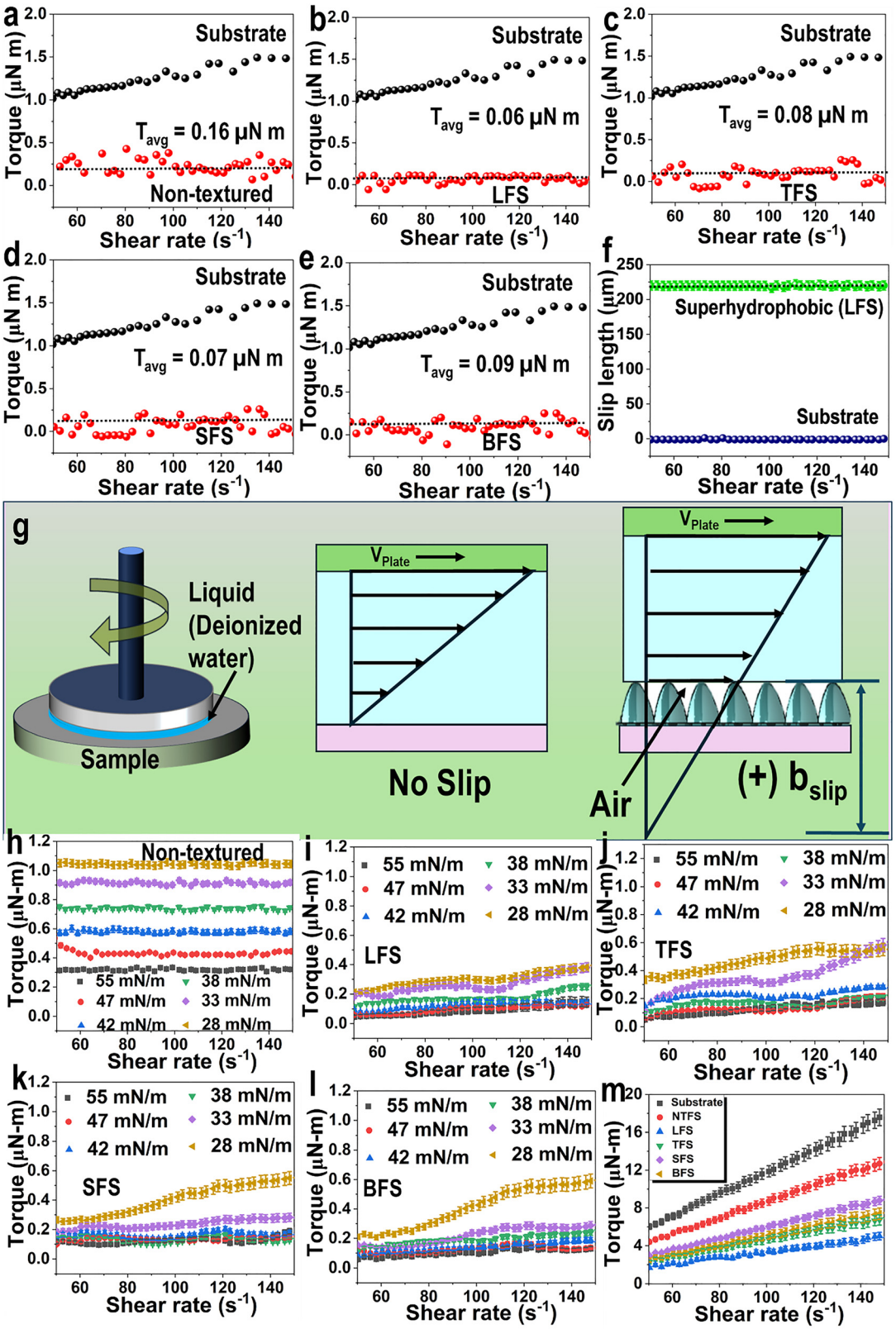

Fig. 6 Investigation of drag behavior showing the variation (a)–(e) in driving torque for non-textured and textured samples, including LFS, TFS, SFS, and BFS, respectively, and (f) slip length as a function of the shear rate for LFS. (g) Schematic illustrating the concept of slip length in flat and enhanced slip length in superhydrophobic coatings. Driving torque measured on (h) non-textured (NTFS) and textured (i) LFS, (j) TFS, (k) SFS, and (l) BFS super-repellent samples against low surface tension liquids. (m) Driving torque measurement against oil (viscosity = 29 mPa s and surface tension = 33 mN m^{-1}) for the substrate and all superhydrophobic coatings.

length (δ) is the measure of a pure air layer of thickness b and difference of viscosities of liquid and air (μ_l and μ_a), as shown in eqn (7):

$$\delta = b\left(\frac{\mu_l}{\mu_a} - 1\right) \quad (7)$$

For a composite interface, the average slip length is measured in co-relation with the liquid–air interface ($1 - f_{sl}$), and is given by eqn (8):[25]

$$\delta = b\left(\frac{\mu_l}{\mu_a} - 1\right)(1 - f_{sl}) \quad (8)$$

From eqn (8), the thickness of the air layer in the LFS sample can be estimated as 5 μm, considering the experimentally determined slip length.

The drag behaviour of all superhydrophobic samples was tested against liquids with different surface tensions, consisting of water-ethanol mixtures ranging from 55 mN m^{-1} to 28 mN m^{-1}. A comprehensive study was conducted to determine the effect of surface tension on drag behaviour *via* torque measurement. Fig. 6(h)–(l) shows torque with respect to shear rate for non-textured and textured samples. The graphs clearly show that the bioinspired additive textures lowered the torque compared to non-textured coatings for liquids of different surface tensions. As expected, higher torque values were recorded for all low surface tension liquids and superhydrophobic coatings. The liquid with the lowest surface tension of 28 mN m^{-1} displayed an average torque value of approximately 1.03 μN m for the non-textured coating. Among the textured coatings, an average torque of 0.28 μN m was recorded for the LFS sample, followed by SFS, BFS, and TFS, with an average torque of 0.40 μN m, 0.41 μN m, and 0.47 μN m, respectively. LFS has shown a 3.6 times lower average torque as compared to the non-textured coating, which indicates the high stability of the entrapped air layer in the developed textures.

The potential of these superhydrophobic coatings was further explored for practical applications. Considering the high energy consumption in oil pipeline transportation, torque was measured for oil with a viscosity of 29 mPa.s and surface tension of 33 mN m^{-1} for substrate, non-textured, and textured coatings. The high viscosity fluids imposed a high drag on the surface, as seen in Fig. 6(m), and the samples displayed high torque values compared to water. Also, the slope linearly increased with increase in shear rate. The lowest average torque against oil was displayed by LFS, followed by TFS, BFS, and SFS. All the textured coatings demonstrated lower torque than the non-textured sample and substrate.

The developed coatings with superhydrophobicity demonstrate oleophobic characteristics. The three-tier hierarchal roughness achieved through a combination of additive textures and flame spraying results in an enhanced air-fraction. The composite at the interface creates a non-uniform flow-field and allows liquid to drag over the solid tips and air interface. Among all the textured coatings, minimum contact was achieved with the LFS sample. That is, the superhydrophobic solid tips only interacted with the liquid layer, resulting in superior drag reduction for water, low surface tension liquids, and oil.

3.5 Corrosion and immersion behavior

The corrosion behaviour of the substrate, non-textured, and textured flame-sprayed samples was investigated in 3.5% NaCl solution. Fig. 7(a) shows the potentiodynamic polarization curves fitted by Tafel extrapolation. The substrate demonstrated the highest corrosion current density of 1.5 μA cm^{-2}, followed by NTFS (1.2 μA cm^{-2}). The textured samples exhibited increased corrosion resistance, with the lowest corrosion current density of 0.3 μA cm^{-2} for LFS, subsequently followed by TFS (0.7 μA cm^{-2}). For the BFS and SFS coatings, there were slightly high corrosion current density values of 1 μA cm^{-2} and 0.9 μA cm^{-2}, respectively. Further the corrosion behaviour was analyzed by electrochemical impedance spectroscopy (EIS).

The Nyquist plot in Fig. 7(b) shows high polarization resistance for LFS, as depicted by the highest semicircular arc, indicating superior corrosion resistance. The lowest semicircular arc was displayed by the substrate, followed by NTFS. In the Bode phase angle-frequency plots in Fig. 7(c), a negative phase angle shift occurred for all the non-textured and textured superhydrophobic samples at lower frequencies, and sustained negative phase angles occurred at higher frequencies, except for BFS. The LFS and TFS samples approached near to ideal capacitor behaviour by reaching a -80° phase angle, which indicated increased corrosion resistance. The substrate and BFS sample underwent high corrosion as the phase angle at higher frequencies approached 0°. Similarly, the LFS and TFS samples show high impedance resistance in Fig. 7(d), indicating superior corrosion resistance.

Fig. 7(e) explains the mechanism of corrosion in a flat substrate, where the electrolyte is in direct contact with a metal surface and a superhydrophobic sample. The reduced solid–liquid contact prevents the direct interaction of electrolyte and surface. Simultaneously, nanostructures induced a high negative capillary pressure, resisting the penetration of electrolyte and corrosive Cl^- ions. The entrapped air between the cavities acts as a dielectric, limiting the ion exchange.

Multiple energy barriers for electrolyte penetration originate from multi-order hierarchal structures. However, although the BSF sample is superhydrophobic in nature, it continued to exhibit poor corrosion behaviour. This indicates that the surface geometry at a macro-scale also plays a significant role in determining corrosion behaviour. The hill-like topography in LFS initially allowed minimum contact of solid with electrolyte. After prolonged exposure, open rhombus-shaped pits formed between the hills to prevent the trapping of electrolyte at valley-dominated regions. Even the abraded LFS sample exhibited a low corrosion current density of 0.34 μA cm^{-2}, which is similar to the corrosion current density of fresh (without abrasion) coating (0.3 μA cm^{-2}), which was attributed to the unique self-regeneration trait of the coating. Fig. S1(b) shows the potentiodynamic polarization curve of an abraded sample.

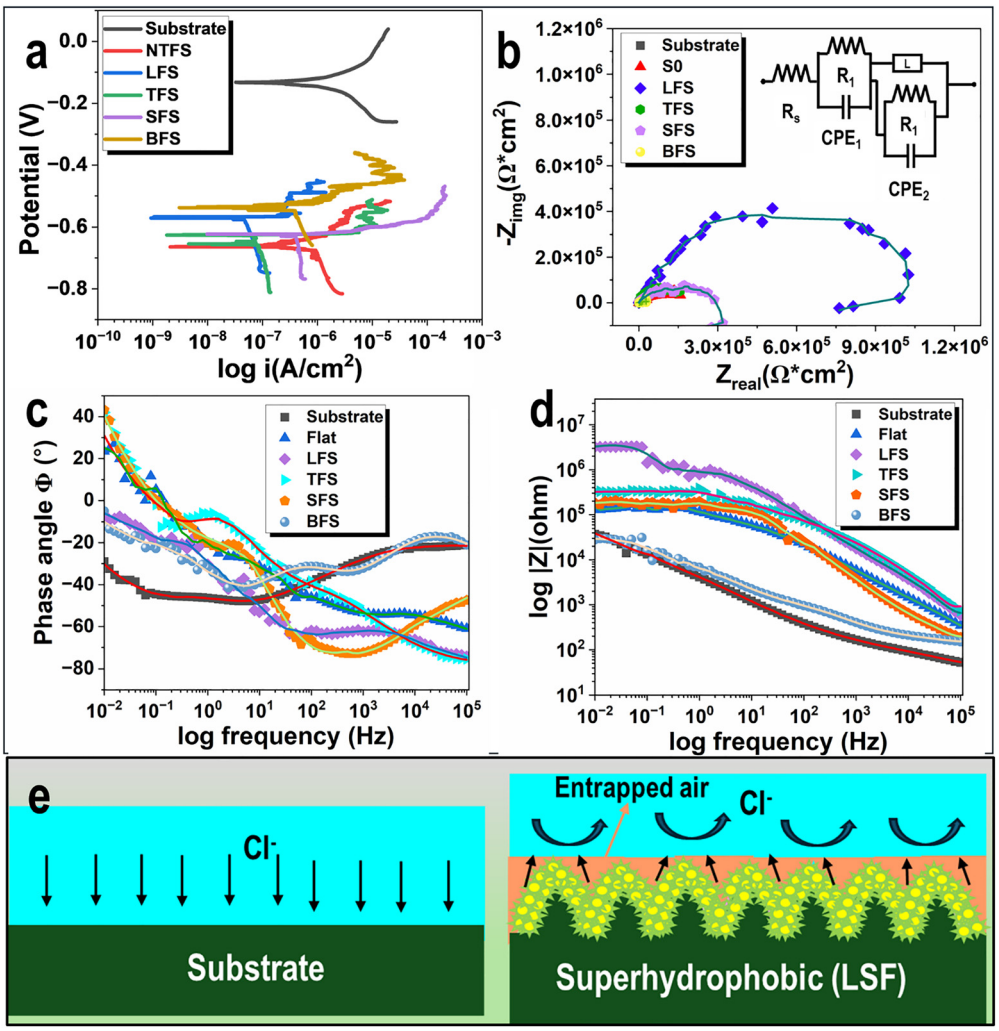

Fig. 7 The corrosion behavior of the substrate, and the NTFS, LFS, TFS, SFS, and BSF superhydrophobic samples is depicted through (a) potentiodynamic polarization results and (b) Nyquist plots with electrical equivalent circuit in the inset, and (c) and (d) Bode plots. (e) Schematic explaining the interaction of aggressive chloride ions with the substrate and superhydrophobic sample where entrapped air acts as an insulating medium for ion exchange.

In the case of BSF, there is greater solid–electrolyte interaction of the rectangular ridges, and the small interconnected ridges create rectangular closed pits. Once penetrated, the electrolyte accumulates in the macro-sized rectangular pockets, and these cavities act as reservoirs, prolonging liquid–solid interaction and exacerbating corrosion. In addition, the resilience of samples was investigated against high-impact waves in a wave simulator. This dynamic immersion test was performed by suspending samples against waves, and after regular intervals, the dynamic contact angles and sliding angles were measured (Fig. 8(a)–(e)).

The LFS sample sustained superhydrophobicity for 250 minutes, followed by TFS for 170 minutes. In contrast, the NTFS and BSF samples retained high contact angles for only 30 minutes and 60 minutes, respectively. The samples also demonstrated superior performance in the outdoor weathering test. The LFS sample displayed high contact angles even after 9 months of exposure, sustaining extreme weather conditions (rainfall of 285 mm, humidity (38% to 92%), high and low temperature (48 °C to 5 °C), and wind (3.4 mph to 10.3 mph)), as shown in Fig. 8(f).

3.6 Anti-staining behavior

The anti-staining behavior of superhydrophobic samples against coffee, tea, juice, tomato sauce, and oil as staining liquids was investigated. The LFS and BFS coatings were selected for evaluation of anti-staining behaviour. LFS exhibited the highest contact angles, while among the textured coatings, the contact angle for BFS was slightly lower. However, because of their superhydrophobic nature, both coatings demonstrated superior resistance to staining. The samples repelled all of these liquids at a sliding angle of 5° with no stains recorded, as seen in Fig. 9(a)–(e).

In Fig. 9(e), the samples exhibited oil repellency against liquids with a surface tension of 33 mN m^{-1}, demonstrating

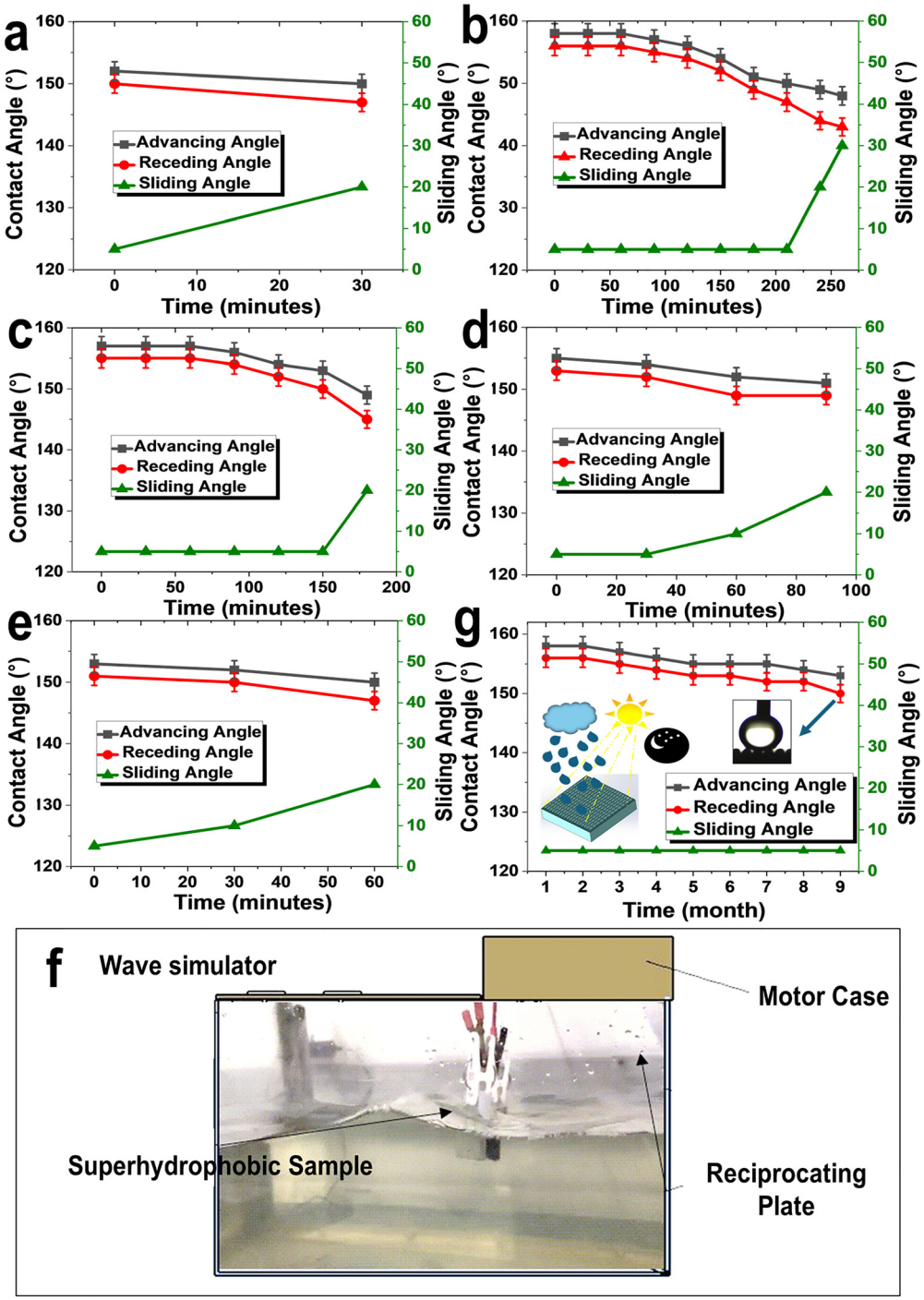

Fig. 8 Change in contact angles during exposure to impacting waves of simulated seawater in the wave simulator for (a) NTFS, (b) LFS, (c) TFS, (d) SFS, and (e) BFS. (f) Setup of the wave simulator, which is designed to study the stability of superhydrophobic coatings under wave impact. (g) Static contact angle measurement of the LFS sample exposed to an outdoor weathering test.

the oleophobic nature of the textured coatings. This trait minimizes viscous drag and flow resistance caused by oil adhesion, thereby contributing to reduced energy loss and improved fuel efficiency in fluid transport systems. Also, it contributes to reduced oil deposition in pipelines, valves, and processing equipment. This capability further mitigates the risk of fire hazards commonly associated with oil accumulation on metallic surfaces. In addition, the demonstrated ability of these textured coatings to repel liquids over a wide viscosity range underscores their functional robustness and opens new avenues for versatile, multipurpose deployment.

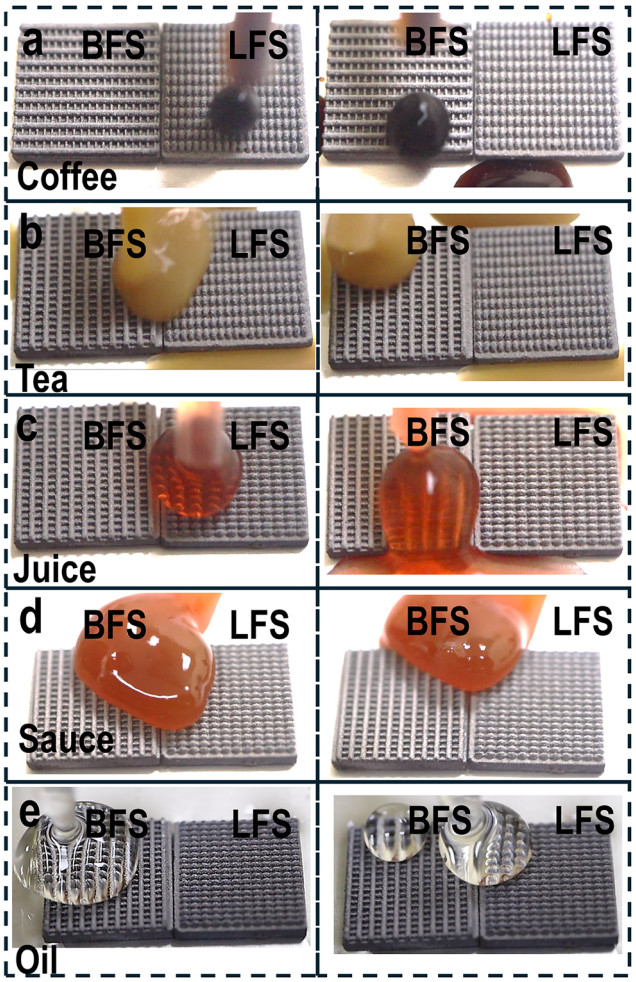

Fig. 9 Anti-staining behaviour of LFS- and BFS-textured superhydrophobic samples exposed to different stain-leaving liquids: (a) coffee, (b) tea, (c) juice, (d) sauce, and (e) oil.

4. Conclusion

Bioinspired additively manufactured textures, decorated with micro-nano roughness through aluminium flame spraying, exhibit exceptional superhydrophobicity, drag reduction, and corrosion resistance, and therefore, they are highly advantageous for marine applications. The lotus-inspired flame-sprayed (LFS) texture demonstrated superior performance, achieving a high contact angle (approximately 158°) and ultra-low adhesion of 2.8 μN, outperforming natural lotus leaves. This design significantly reduces solid–liquid interaction, promoting efficient de-wetting and minimizing resistance for water, low surface tension liquids, and oils. Notably, an average torque of 0.06 μNm was recorded for LFS against water, which was 21 times lower than that of the substrate, emphasizing its potential for fuel and water transportation.

Furthermore, its exceptional anti-corrosion properties, marked by the lowest corrosion current density (0.3 μA cm^{-2}) and high polarization resistance, enhance its long-term durability in harsh environments. In contrast, the BFS sample showed higher corrosion susceptibility due to macropit formation, leading to water entrapment upon penetration. These engineered surfaces represent a significant advancement in surface technology, offering robust self-regenerative capabilities and enhanced durability, and thus, they are a promising innovation for marine and industrial applications.

Author contributions

Aaishwarika Raj Sharma: writing – review and editing, writing – original draft, visualization, validation, methodology, investigation, formal analysis, data curation, conceptualization. Harpreet Arora: writing – review and editing, writing – original draft, supervision, project administration, funding acquisition, formal analysis. Harpreet Singh Grewal: writing – review and editing, writing – original draft, validation, supervision, resources, project administration, methodology, formal analysis, conceptualization.

Conflicts of interest

The authors declare that they have no known competing financial interests or personal relationships that could have appeared to influence the work reported in this paper.

Data availability

The data supporting this article will be made available on request.

Supplementary information (SI) is available. See DOI: https://doi.org/10.1039/d5ma01236h.

References

1 H. K. Webb, R. J. Crawford and E. P. Ivanova, Wettability of natural superhydrophobic surfaces, *Adv. Colloid Interface Sci.*, 2014, **210**, 58–64.
2 T. Darmanin and F. Guittard, Superhydrophobic and superoleophobic properties in nature, *Mater. Today*, 2015, **18**(5), 273–285.
3 R. Hensel, C. Neinhuis and C. Werner, The springtail cuticle as a blueprint for omniphobic surfaces, *Chem. Soc. Rev.*, 2016, **45**(2), 323–341.
4 A. R. Sharma, H. Arora and H. S. Grewal, Facile Synthesis of Nanostructured Self-Regenerative Superhydrophobic Coatings, *Adv. Eng. Mater.*, 2024, 2401279.
5 P. Pathak, P. Kaur and H. S. Grewal, Rice husk-derived self-healing superhydrophobic films using solvent-less approach for drag reduction and oil absorption behaviour, *Ind. Crops Prod.*, 2024, **222**, 119812.
6 B. Nomeir, S. Lakhouil, S. Boukheir, M. A. Ali and S. Naamane, Recent progress on transparent and self-cleaning surfaces by superhydrophobic coatings deposition to optimize the cleaning process of solar panels, *Sol. Energy Mater. Sol. Cells*, 2023, **257**, 112347.

7 A. R. Sharma, P. Pathak, H. Arora and H. S. Grewal, Flame-sprayed self-regenerative scalable superhydrophobic coating for anti-drag and anti-corrosion applications, *Mater. Today Commun.*, 2025, **44**, 112174.
8 H. Zheng, S. Chang and Y. Zhao, Anti-Icing & Icephobic Mechanism and Applications of Superhydrophobic/Ultra Slippery Surface, *Prog. Chem.*, 2017, **29**(1), 102–118.
9 R. E. Lobo, B. Guzmán, P. A. Orrillo, C. C. Domínguez, L. E. Jimenez and M. I. Torino, Corrosion: Basics, Adverse Effects and Its Mitigation, in *Sustainable Food Waste Management: Anti-corrosion Applications*, ed. R. Aslam, M. Mobin, and J. Aslam, Springer Nature, Singapore, 2024, pp. 3–22.
10 Y.-y Lau, Q. Chen, M. C.-P. Poo, A. K. Y. Ng and C. C. Ying, Maritime transport resilience: A systematic literature review on the current state of the art, research agenda and future research directions, *Ocean Coastal Manage.*, 2024, **251**, 107086.
11 D. Clarke, P. Chan, M. Dequeljoe, Y. Kim and S. Barahona, *CO_2 emissions from global shipping, 2023.*
12 A. Sharma, H. Arora and H. S. Grewal, Tuning surface morphology through facile microwave assisted hot water treatment, *Mater. Sci. Eng., B*, 2025, **314**, 118063.
13 V. Athulya, S. C. Vanithakumari, A. R. Shankar and S. Ningshen, Electrodeposition of myristate based superhydrophobic coatings on steel with enhanced corrosion resistance and self-cleaning property, *Surf. Coat. Technol.*, 2024, **489**, 131114.
14 T. Rakheja, P. Pathak and H. S. Grewal, Facile fabrication of super-slippery and transparent glass with anti-fogging and self-cleaning characteristics, *Mater. Lett.*, 2024, **366**, 136506.
15 P. Pathak and H. S. Grewal, Solvent-free synthesis of self-regenerative superhydrophobic film from silicone waste with drag-reduction and selective oil absorption behaviour, *Chem. Eng. J.*, 2024, **487**, 150479.
16 N. Kehagias, A. Francone, M. Guttmann, F. Winkler, A. Fernández and C. M. Sotomayor Torres, Fabrication and replication of re-entrant structures by nanoimprint lithography methods, *J. Vac. Sci. Technol., B: Nanotechnol. Microelectron.:Mater., Process., Meas., Phenom.*, 2018, **36**(6), 06JF01.
17 D. Herzog, V. Seyda, E. Wycisk and C. Emmelmann, Additive manufacturing of metals, *Acta Mater.*, 2016, **117**, 371–392.
18 T. D. Ngo, A. Kashani, G. Imbalzano, K. T. Q. Nguyen and D. Hui, Additive manufacturing (3D printing): A review of materials, methods, applications and challenges, *Composites, Part B*, 2018, **143**, 172–196.
19 J. Sun, W. Wang, Z. Liu, B. Li, K. Xing and Z. Yang, Study on selective laser melting 316L stainless steel parts with superhydrophobic surface, *Appl. Surf. Sci.*, 2020, **533**, 147445.
20 H. Zhang, D. Gu, C. Ma, M. Xia and M. Guo, Surface wettability and superhydrophobic characteristics of Ni-based nanocomposites fabricated by selective laser melting, *Appl. Surf. Sci.*, 2019, **476**, 151–160.
21 S. Mekhiel, P. Koshy and M. A. Elbestawi, Additive texturing of metallic surfaces for wetting control, *Addit. Manuf.*, 2021, **37**, 101631.
22 A. R. Sharma, H. Arora and H. S. Grewal, Facile Synthesis of Nanostructured Self-Regenerative Superhydrophobic Coatings, *Adv. Eng. Mater.*, 2024, 2401279.
23 C. S. Yang, J. S. Kim, J. Woo Choi, M. H. Kwon, Y. J. Kim, J. G. Choe and G.-T. Kim, XPS Study of Aluminum Oxides Deposited on PET Thin Film, *J. Korean Soc. Atmos. Environ.*, 2000, **6**, 149.
24 C.-S. Yang, *et al.*, XPS Study of Aluminum Oxides Deposited on PET Thin Film XPS Study of Aluminum Oxides Deposited on PET Thin Film, *J. Ind. Eng. Chem.*, 2000, **6**, 149–156.
25 M. Nosonovsky and B. Bhushan, Hierarchical roughness optimization for biomimetic superhydrophobic surfaces, *Ultramicroscopy*, 2007, **107**(10), 969–979.
26 M. Li, Y. Li, F. Xue and X. Jing, A robust and versatile superhydrophobic coating: Wear-resistance study upon sandpaper abrasion, *Appl. Surf. Sci.*, 2019, **480**, 738–748.
27 S. Meng, *et al.*, Preparation and properties of high abrasion resistant superhydrophobic coating on the PCB, *Colloids Surf., A*, 2024, **689**, 133674.
28 Y. Zhang, *et al.*, Corrosion-resistant superhydrophobic composite coating with mechanochemical durability, *Colloids Surf., A*, 2024, **703**, 135186.
29 A. Maali and B. Bhushan, Measurement of slip length on superhydrophobic surfaces, *Philos. Trans. R. Soc., A*, 2012, **370**(1967), 2304–2320.